

ARCHITECTED LATTICE SANDWICH STRUCTURES FOR LIGHTWEIGHT IMPACT AND ENERGY ABSORPTION APPLICATIONS

George Catalin Cristea[1], Marius Pop[1], Adriana Stefan[1], Botan Mihail[1] & Alina Dragomirescu[1]

[1]INCAS – National Institute for Aerospace Research "Elie Carafoli", B-dul Iuliu Maniu 220, Bucharest 061126, Romania

Abstract

Additive manufacturing has enabled the creation of a class of architected cellular materials in which the macroscopic mechanical response is governed by deliberately designed geometry. The present work provides an experimental evaluation of the influence of cellular topology and functional gradation on the quasi-static compression and low-velocity impact behaviour of sandwich cores. Four architectures were investigated: a uniform gyroid (G14-14), a linear graded gyroid (G20-10), a uniform re-entrant honeycomb (RE) and a graded re-entrant honeycomb (RE var). All cores were fabricated from PLA as 60 × 60 × 60 mm specimens at a constant overall relative density of approximately 0.31 and were assembled in sandwich configurations with aramid/epoxy face sheets.

The experimental program included quasi-static compression and instrumented drop-weight impact at an incident energy of 100 J. Under quasi-static compression, the gyroid cores exhibited higher stiffness, higher plateau stress, and superior specific energy absorption compared to the re-entrant architectures. The specific energy absorption up to 50% of nominal strain reached 3.66–4.09 J/g for the gyroid cores, approximately double the 1.88–1.94 J/g obtained for the re-entrant cores. Functional grading attenuated the initial peak stress by 19% in the gyroid family and by 60% in the re-entrant family, while promoting a more progressive post-peak response associated with a spatially controlled collapse sequence.

The impact response was consistent with the quasi-static compression behaviour. The G20-10 graded gyroid exhibited the highest and most repeatable peak force upon impact, 12.49 ± 0.33 kN, with a maximum displacement of 49.73 ± 1.12 mm and localized crater depths of 3.48–4.11 mm, while maintaining overall core integrity. The G14-14 uniform gyroid achieved a lower peak force of 10.28 ± 1.09 kN and a maximum displacement of 54.03 ± 1.20 mm, but exhibited buckling and partial detachment of the Kevlar/PLA top face. In contrast, the re-entrant architectures failed by complete structural collapse. The re-entrant uniform structure exhibited a low peak force of 5.35 ± 0.50 kN but a large maximum displacement of 90.77 ± 3.29 mm. The graded re-entrant structure improved repeatability and reduced the maximum displacement to 39.82 ± 1.26 mm, but still failed by complete collapse.

These results demonstrate that the network topology dictates the dominant energy absorption mechanism, while the cell size grading controls the spatial evolution of collapse and the balance between transmitted load, deformation stroke, and residual integrity. Among the architectures investigated, the G20-10 graded gyroid offered the best overall compromise between quasi-static load capacity, localized impact resistance, and post-impact structural preservation, making it a promising candidate for lightweight sandwich structures intended for impact and energy absorption applications.

Keywords: cellular materials; energy absorption mechanisms; additive manufacturing; lightweight protective systems; functionally graded

1. Introduction

Lightweight and damage-tolerant structures remain a central challenge in aeronautical engineering, particularly for components exposed to impact, accident-related loads, and localized dynamic events [1]. Helicopters, fixed-wing aircraft, and advanced aerial platforms are routinely subjected to low-speed impacts resulting from debris strikes, maintenance operations, and accidental contact, as well as more severe dynamic loads associated with emergency landings or hostile environments. Sandwich structures with energy-absorbing cores address this need by combining high stiffness-to-weight ratios with improved energy dissipation [2], [3].

Recent advances in additive manufacturing have enabled the creation of architectural network materials whose mechanical response is tailored by geometry, rather than by material composition alone [3], [4], [5], [6]. Unlike conventional honeycombs or polymeric foams, additively manufactured

networks allow precise control over the topology, cell size, wall thickness, and spatial gradation of properties [7]. This design freedom is particularly relevant for protective aeronautical structures, where limiting peak loads, promoting progressive collapse, and reducing damage transmission to surrounding components are critical performance objectives.

Two complementary cell concepts are considered in this work. Triple Periodic Minimum Surface (TPMS) topologies, and in particular the gyroid, provide smooth, continuous walls with predominantly tensile-dominated load transfer, favorable fabricability, and stable post-failure behaviour [8], [9], [10]. Re-entrant (auxetic) honeycomb topologies, characterized by a negative in-plane Poisson's ratio, collapse through bending-dominated support mechanisms and develop reduced transmitted loads over long spans. For each topology, a uniform configuration and a functionally graded configuration were investigated, with the cell size varying along the loading direction, resulting in four architectures. Gradation was introduced to allow spatial control of stiffness and collapse sequence.

This study investigates the quasi-static compression and low-velocity impact response of four architected lattice cores, fabricated as polymer (PLA) specimens at constant overall relative density and assembled into sandwich specimens with aramid/epoxy composite face sheets. The use of a polymer core at this stage isolates geometry-driven mechanisms, which are intended to be transferred to higher-performance metal systems fabricated by powder bed fusion [11], [12], [13], [14], [15], [16].

2. Materials and Methods

2.1 Lattice architectures

Four cubic lattice cores with nominal dimensions of 60 × 60 × 60 mm were designed, spanning two topologies (gyroid TPMS and re-entrant honeycomb), each in a uniform and a functionally graded variant (Figure 1). The uniform gyroid (G14-14) used a constant cell size of 14 mm throughout the specimen height. The graded gyroid (G20-10) used a cell size varying linearly along the loading direction from 20 mm to 10 mm. The re-entrant cores were produced in a uniform configuration (RE) and in a height-graded configuration (RE var). A constant global relative density of approximately 0.31 was targeted across all four architectures in order to isolate the influence of topology and grading from that of mass.

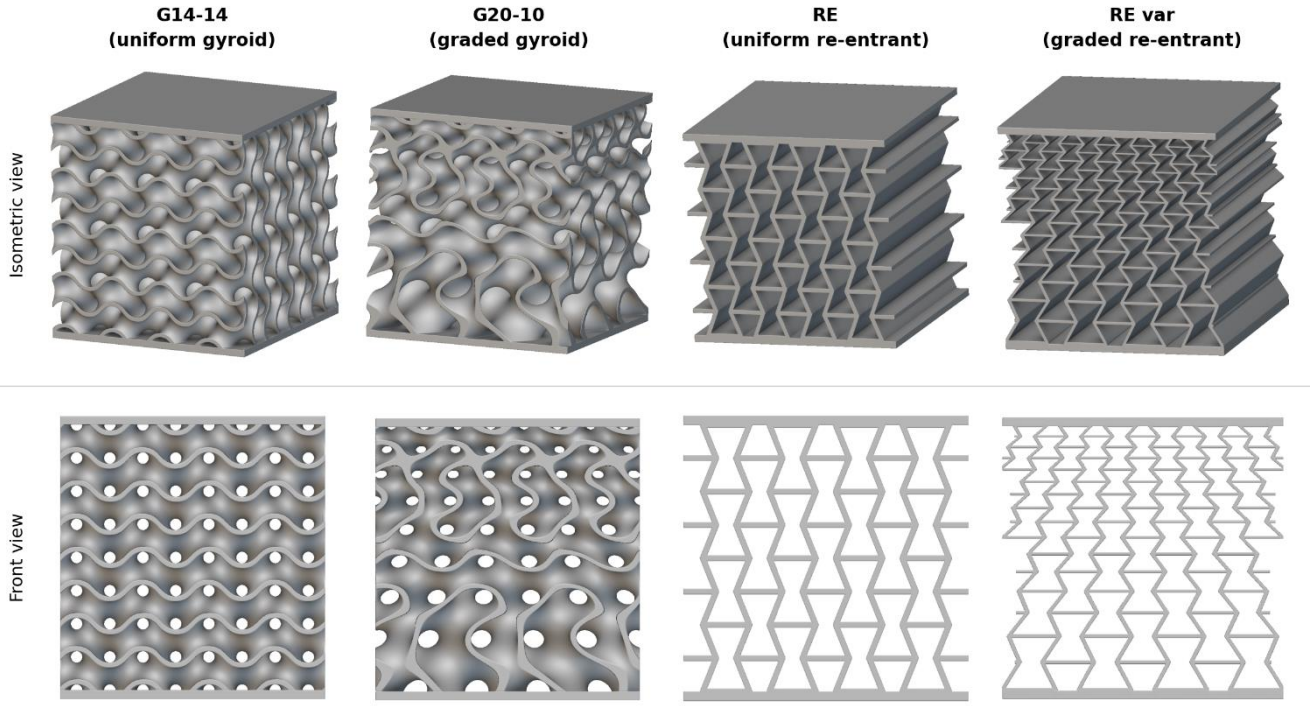


Figure 1 – The four lattice core architectures: isometric views (top) and front views (bottom).

2.2 Additive manufacturing and mass verification

The lattice cores were fabricated by material extrusion (fused filament fabrication) on a Bambu Lab

P2S desktop system using BASF Ultrafuse PLA filament of 1.75 mm diameter. To minimize moisture induced extrusion defects and porosity, the filament was dried for 24 h at 45 °C immediately prior to printing. The cores were processed with a nozzle temperature of 210 °C, a layer height of 0.2 mm and 100% infill, the latter ensuring that the solid fraction of the printed struts and walls was fully dense and that the global relative density was dictated solely by the lattice topology rather than by internal slicer-generated porosity [17], [18].

The constant relative density of the four architectures was verified gravimetrically. For a fully solid PLA cube of identical envelope (216 cm³, $\rho_{PLA} \approx 1.24$ g/cm³, m ≈ 268 g), the measured core masses of 82.56 - 83.01 g correspond to a relative density of $\rho^* \approx 0.31$. This value was consistent across all architectures and exhibited very low intra-group scatter (standard deviations ≤ 0.09 g; Table 1), confirming that topology and grading were the only variables differentiating the specimens, and attesting to the repeatability of the manufacturing route. Six specimens were manufactured for each architecture. Within each architecture, specimens 1 to 3 were allocated to quasi-static compression and specimens 4–6 to low-velocity impact.

Table 1 - Printed core mass per architecture (n = 6 specimens each)

Architecture	Mean mass [g]	St. dev. [g]
G14-14 (uniform gyroid)	82.79	0.09
G20-10 (graded gyroid)	82.93	0.07
RE (uniform re-entrant)	82.97	0.03
RE var (graded re-entrant)	82.61	0.04

2.3 Composite face sheets and sandwich assembly

The composite face sheets were laminated from 10 plies of aramid (Kevlar) 2/2 twill fabric with an areal density of 173 g/m² in a symmetric [0/45/0/45/0]s stacking sequence, impregnated with SikaBiresin CR82 epoxy resin and CH80-2 hardener. The lay-up was consolidated as a single 300 × 400 mm plate under a 60 kN press load for 24 h at room temperature. Individual 60 × 60 mm face sheets were then cut from the cured plate using a Wazer abrasive waterjet system, which produced clean edges without thermally affecting the laminate. After cutting, the face sheets were dried in an oven at 40 °C for 24 h, then weighed and dimensionally measured.

The finished face sheets had a mean thickness of 2.0 mm (range 1.96 - 2.03 mm) and a mean mass of 9.6 g (range 9.38 - 9.79 g). The constituent content of each face sheet was determined from its measured mass and dimensions, the nominal fabric areal density, and the constituent densities ρ_f (fiber) and ρ_m (matrix). The theoretical fiber mass is obtained from the fabric areal density and the measured in-plane area:

$$m_f = n \cdot \rho_A \cdot A \tag{1}$$

from which the fiber and matrix mass fractions follow: area:

$$W_f = \frac{m_f}{mW_m} = 1 - W_f = \frac{m - m_f}{m} \tag{2}$$

Referring the fiber and matrix volumes to the measured laminate volume $V = A \cdot t$ gives the fiber and matrix volume fractions, and the void content by closure:

$$V_f = \frac{m_f}{\rho_f \cdot A \cdot t} \tag{3}$$

$$V_m = \frac{m - m_f}{\rho_m \cdot A \cdot t} \tag{4}$$

$$V_v = 1 - V_f - V_m \quad (5)$$

Using ρ_f = 1.44 g/cm³ for the aramid fiber and ρ_m = 1.15 g/cm³ for the cured epoxy, the finished face sheets (mean thickness 2.0 mm, mean mass 9.6 g) exhibited a fiber mass fraction of W_f = 65.9 ± 1.2%, a fiber volume fraction of V_f = 60.3 ± 1.1%, and a void content of Vv ≈ 0.6%, confirming effective consolidation and repeatable laminate quality across all specimens.
Face sheets were bonded to the top and bottom surfaces of each printed core to form the sandwich specimens. For the impact tests, both the front (impacted) and the rear face sheet of every specimen were individually weighed and measured prior to assembly, so that the local areal properties at the impact site were known for each test.

2.4 Quasi-static compression

Quasi-static compression tests were performed on an Instron universal testing machine equipped with a 100 kN load cell, following ASTM D695-08, at ambient conditions. The crosshead speed was 1.3 mm/min up to a 100 N preload, then 5 mm/min until the test stop condition of 40 mm crosshead displacement (corresponding to 66.7% nominal strain) was reached. Nominal stress was computed on the 60 × 60 mm footprint (3600 mm²) and nominal strain as $\varepsilon = \delta/H_0$ with $H_0 = 60$ mm. The initial stiffness was evaluated by a linear fit in the 0.5 - 1.5% strain range, the initial peak stress as the maximum stress below 10% strain, and the plateau stress as the mean stress in the 20 - 50% strain band. The absorbed energy was computed by trapezoidal integration of the force - displacement response (Equation 6) up to 50% nominal strain, and the specific energy absorption (SEA) by normalizing to the printed core mass, the face sheets being identical across architectures.

$$U_{50} = \sum_{i=1}^{m-1} \frac{F_i + F_{i+1}}{2} (\Delta_{i+1} - \Delta_i) \quad (6)$$

2.5 Low-velocity impact

Instrumented drop-weight impact tests were performed on a CEAST 9350 tower fitted with a hemispherical instrumented tup of 16 mm diameter. The impactor carriage had a total mass of 10.324 kg and was released from a drop height of 988 mm, corresponding to an impact velocity of 4.40 m/s and a nominal incident energy of 100 J. Each sandwich specimen was positioned on a flat rigid base and secured with double-sided adhesive tape to prevent lateral displacement and ensure that the impact occurred at the intended central location of the face sheet. An anti-rebound system was engaged to arrest the impactor after the first contact and thereby preclude secondary impacts, so that the recorded response corresponds to a single, well-defined impact event.
The force - time history was acquired by the instrumented tup, and the velocity, displacement and absorbed energy were obtained by successive numerical integration of the force signal under the measured velocity. The contact event was delimited by a 50 N force threshold, and the peak force, the maximum displacement during contact and the contact duration were extracted for each specimen for comparison across architectures.

3. Results and Discussion

3.1 Quasi-static compressive response

The quasi-static compressive behaviour of PLA lattice-core specimens is shown in Figure 2 in terms of nominal compressive stress versus nominal compressive strain. All architectures exhibited the three regimes characteristic of cellular solids under compression: an initial quasi-linear regime, a plateau associated with progressive cell collapse, and a final densification regime marked by a steep stress rise. The group-mean curves of Figure 2 are accompanied by min - max bands of the individual tests, illustrating the repeatability of the response.
The two topologies produced significantly different responses. The gyroid cores were considerably stiffer and stronger, with an initial stiffness of approximately 174 - 178 MPa and an initial peak stress of 3.45 - 4.28 MPa, reflecting the predominantly tensile load transfer of the continuous walls with minimal area. The re-entrant cores, governed by the bending collapse of the inclined struts, were more flexible (≈ 62 - 120 MPa) and developed a much lower plateau. As a result, the gyroid cores absorbed approximately twice the energy of the re-entrant cores in the operationally relevant pre-densification range: the specific energy absorption up to 50% strain reached 3.66 - 4.09 J/g for the

gyroids versus 1.88 - 1.94 J/g for the re-entrant cores (Table 3, Figure 3).

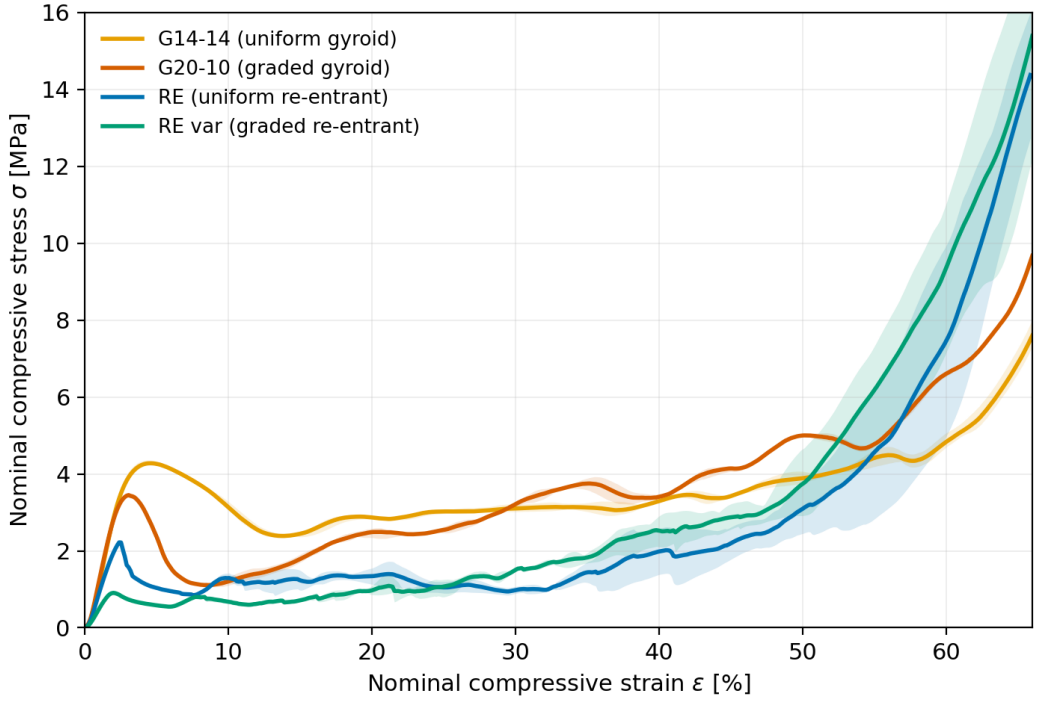


Figure 2 – Nominal stress - strain response in quasi-static compression: group means with min - max bands.

Table 2 – Compression metrics (group mean ± standard deviation, energies up to 50% strain)

Architecture	E [MPa]	σ_{pk} [MPa]	σ_{pl} 20 - 50% [MPa]	SEA_{50} [J/g]
G14-14	178 ± 4	4.28 ± 0.07	3.22 ± 0.08	4.09 ± 0.07
G20-10	174 ± 4	3.45 ± 0.05	3.45 ± 0.03	3.66 ± 0.05
RE	120 ± 2	2.26 ± 0.01	1.61 ± 0.50	1.88 ± 0.46
RE var	62 ± 3	0.91 ± 0.05	2.00 ± 0.22	1.94 ± 0.17

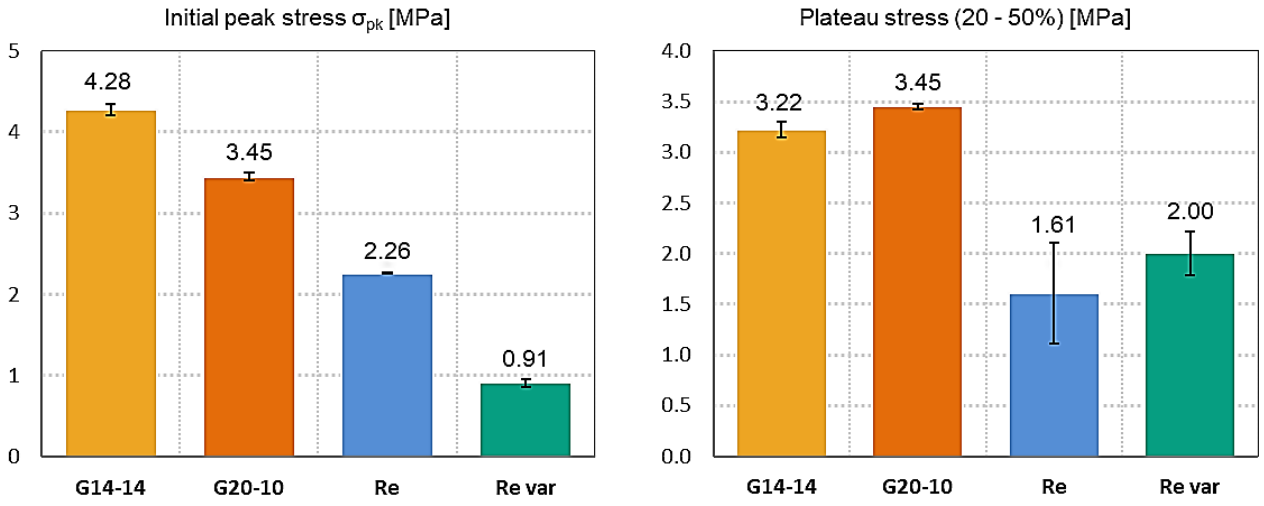


Figure 3 – Initial peak stress and plateau stress of architectures

Within each topology, gradation of cell size along the loading direction reduced the initial peak stress and replaced the post-failure plateau with a progressively ascending one, consistent with a collapse front that initiates in the coarse, flexible cells and propagates toward the fine, stiff cells. In the gyroid family, gradation reduced the initial peak from 4.28 MPa (G14-14) to 3.45 MPa (G20-10), a 19%

reduction, while maintaining a comparable mid-stroke plateau (3.22 → 3.45 MPa). In the re-entrant family, the effect was considerably stronger: gradation reduced the initial peak from 2.26 MPa (RE) to 0.91 MPa (RE var), a 60% reduction, while slightly increasing the mid-stroke plateau (1.61 → 2.00 MPa). This peak load attenuation is directly relevant to sandwich applications, as a lower stress transmitted at the onset of collapse limits the initiation of damage in the composite shells and the protected substructure.

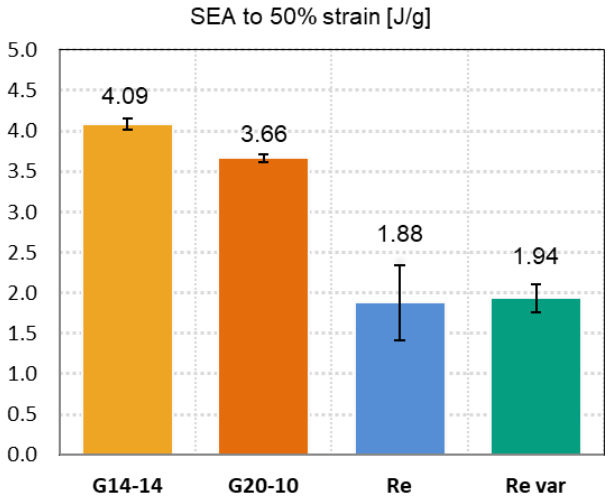


Figure 4 – Specific energy absorption of architectures

The gyroid architectures showed excellent repeatability, while the graded re-entrant architecture exhibited improved repeatability compared with the uniform re-entrant configuration, although larger scatter remained in the plateau region.

3.2 Low-velocity impact response

The force-displacement curves obtained during impact are shown in Fig. 5. The results reveal clear differences between the gyroid and re-entrant architectures. The graded gyroid specimens, G20-10, presented the highest and most repeatable impact force among the configurations analyzed. The peak force varied only slightly between the three specimens, with an average value of approximately 12.49 ± 0.33 kN. The corresponding maximum displacement was 49.73 ± 1.12 mm, while the maximum energy recorded during the test was close to the imposed impact energy, with an average value of 104.97 ± 0.11 J. This response indicates that the graded gyroid architecture offered a high load-bearing capacity under the impact load. The presence of smaller and denser cells in the impact region contributed to a more resistant upper zone, limiting excessive penetration and preventing complete core collapse.

The constant gyroid configuration, G14-14, also exhibited relatively high impact strength, although its peak force was lower than that of G20-10. The average peak force was approximately 10.28 ± 1.09 kN, while the maximum displacement reached 54.03 ± 1.20 mm, as shown in Table 3. Compared to the graded gyroid specimens, the constant gyroid structures allowed slightly larger displacements and exhibited a different damage mechanism. Post-impact inspection revealed bending and partial delamination of the Kevlar/PLA top sheet. This behaviour suggests that, in the absence of a denser lateral impact region, the constant gyroid structure transferred some of the impact load into global bending and delamination of the front sheet, rather than limiting the damage to a localized indentation area.

The re-entrant specimens exhibited significantly different behaviour. The RE configuration showed a large scatter in the recorded impact response. Samples RE_1 and RE_3 reached relatively low peak forces of approximately 4.99 kN and 5.70 kN, respectively, while undergoing large displacements. This indicates a flexible response, associated with severe deformation and collapse of the re-entrant cell walls. However, RE_2 exhibited an abnormally high peak force of approximately 26.68 kN, which is also visible in the force-displacement response shown in Fig. 5 and in the force-time response in Fig. 6. Since the re-entrant samples underwent complete structural collapse, this high peak force was attributed to secondary contact between the impactor and the metallic support after the lattice core failed. Therefore, RE_2 was retained in the raw data set but treated as an outlier when discussing the intrinsic impact response of the RE network. Excluding RE_2, the RE

configuration displayed an average peak force of approximately 5.35 ± 0.50 kN and a maximum displacement of 90.77 ± 3.29 mm. This confirms that the constant re-entrant architecture dissipated the impact energy mainly through large deformations and collapse, but with a significant loss of structural integrity.

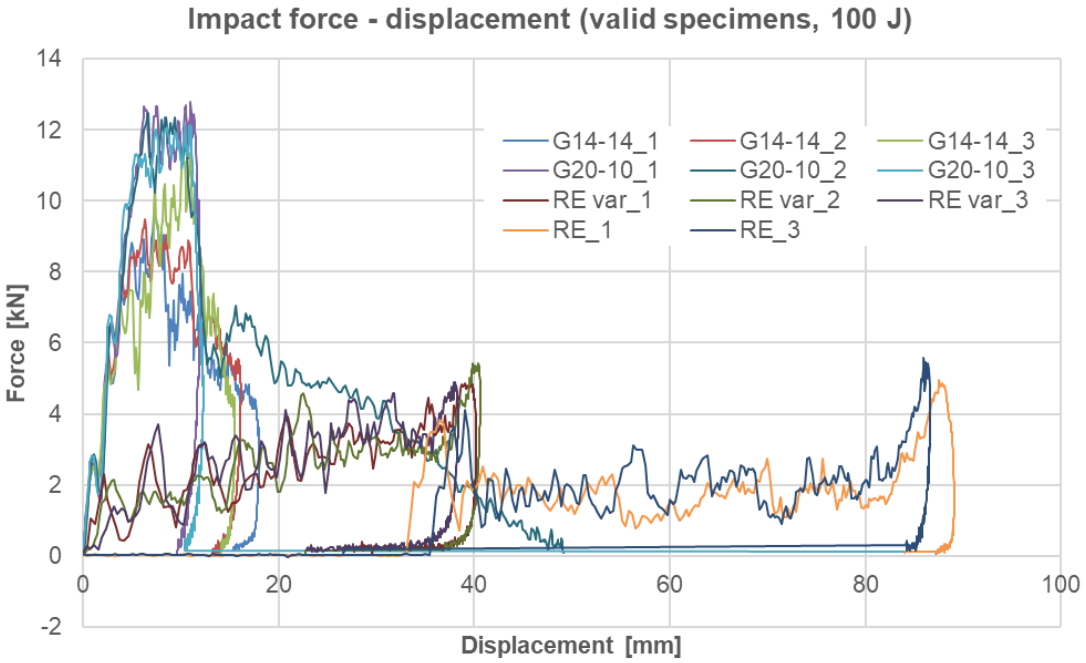


Figure 5 – Impact force - displacement response of the valid specimens.

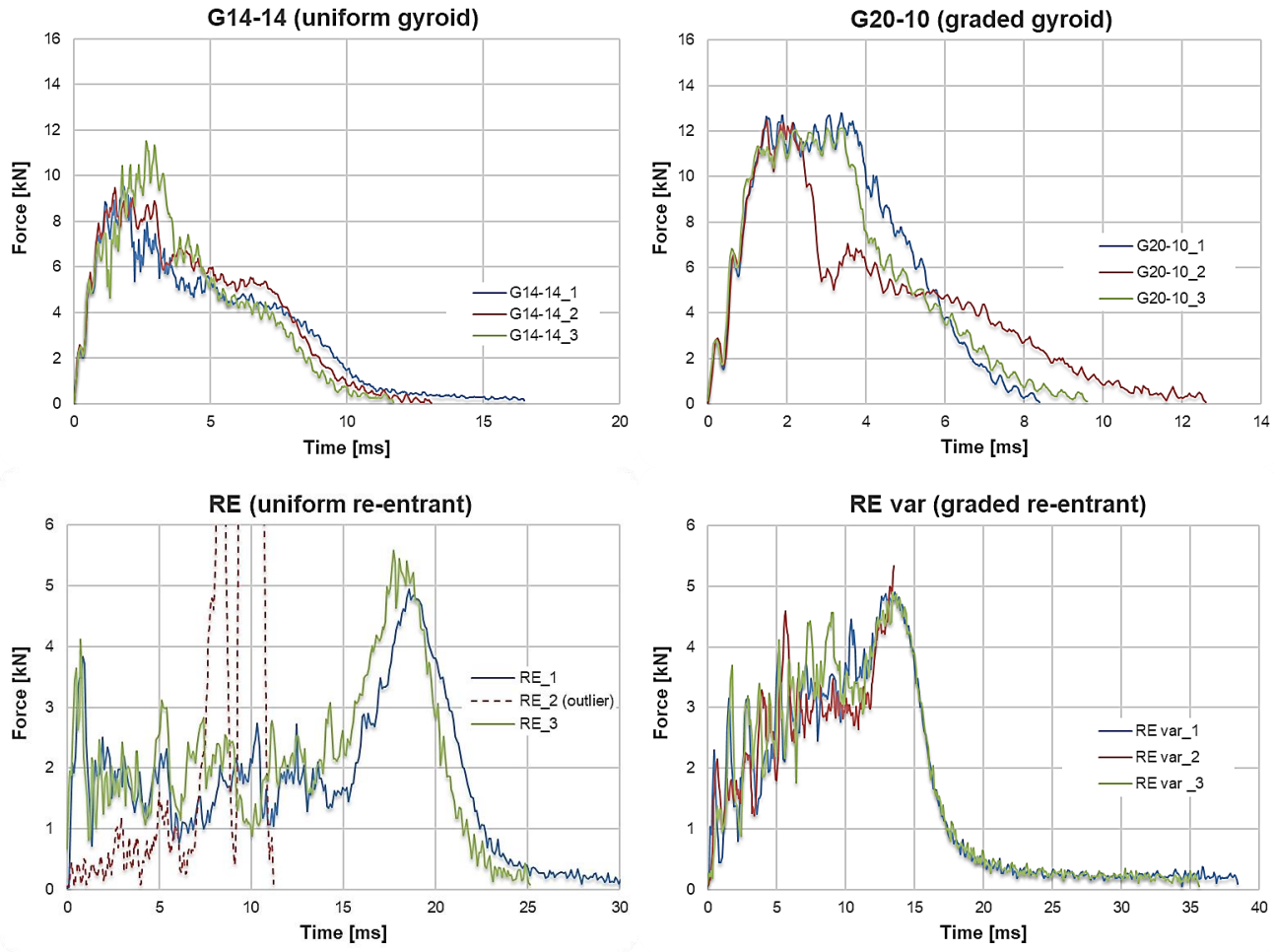


Figure 6 – Impact force–time response per architecture (100 J drop-weight), dashed curves indicate excluded outliers.

The graded re-entrant configuration, RE var, exhibited a more repeatable response than the constant RE structure. The average peak force was approximately 5.12 ± 0.29 kN, while the maximum displacement was 39.82 ± 1.26 mm. Although the peak force was comparable to that of RE, the displacement was considerably smaller, suggesting that the graded re-entrant structure restricted the deformation stroke. However, post-impact observations showed complete destruction of the specimens, indicating that the grading strategy was not sufficient to preserve the overall integrity of the re-entrant architecture under a 100 J impact event. Therefore, the energy was mainly absorbed through the collapse and severe fragmentation of the cell wall.
The main impact parameters obtained for the four configurations are summarized in Table 3. For the RE configuration, the average values are reported excluding the RE_2 specimen.

Table 3 – Impact metrics (group mean ± standard deviation)

Geometry	Specimens	Peak force [kN]	Maximum displacement [mm]	Maximum energy [J]	Main failure mode
G14-14	3	10.28 ± 1.09	54.03 ± 1.20	105.41 ± 0.12	Face bending and partial debonding
G20-10	3	12.49 ± 0.33	49.73 ± 1.12	104.97 ± 0.11	Localized indentation
RE	2	5.35 ± 0.50	90.77 ± 3.29	109.13 ± 0.33	Complete collapse, RE_2 outlier
RE var	3	5.12 ± 0.29	39.82 ± 1.26	103.97 ± 0.13	Complete collapse

Post-impact inspection further confirmed the influence of network topology on the damage pattern. Specimens G20-10 exhibited localized craters on the Kevlar impact face, with measured depths of 3.48 mm, 3.62 mm, and 4.11 mm. The damage remained concentrated primarily around the impact point, and the cellular core retained its overall integrity. This indicates that the graded gyroid architecture was effective in distributing the impact load while restricting overall structural collapse.
Specimens G14-14, in contrast, exhibited more pronounced top sheet buckling. In G14-14_1 and G14-14_2, the Kevlar/PLA top sheet was buckled and partially detached, preventing reliable crater depth measurements. This failure mode suggests that the constant gyroid core provided sufficient strength to avoid complete fragmentation, but the impact energy induced significant local buckling and interface damage at the top face. This supports the conclusion that the graded gyroid configuration provided improved local impact resistance compared to the constant gyroid structure.

3.3 Correlation between quasi-static compression and low-velocity impact response

Comparison of quasi-static compression and low-velocity impact results shows that the two test methods are mutually consistent in identifying the dominant role of network topology and functional gradation on the mechanical response of sandwich specimens. Compression tests provide information about the intrinsic core collapse mechanism, while impact tests reveal how this mechanism is activated under localized dynamic loading and how it affects damage tolerance, penetration resistance, and post-impact integrity.
Under quasi-static compression, both gyroid configurations exhibited higher stiffness, higher plateau stress, and higher specific energy absorption than the re-entrant configurations. This indicates that the continuous TPMS wall network provides a stable load transfer path and an efficient collapse mechanism over a wide range of deformation. The same behaviour was reflected under impact loading. Both gyroid configurations resisted complete structural collapse, while damage remained mainly confined to the upper region of the sandwich specimen. Therefore, the compressive response was consistent with the superior damage tolerance observed for the gyroid cores under impact.
Within the gyroid family, the graded G20-10 architecture exhibited the most favourable impact behaviour, despite the fact that the uniform G14-14 configuration achieved a slightly higher peak initial stress and SEA in quasi-static compression. This apparent difference highlights the importance of considering the full deformation mechanism, rather than just the scalar compression metrics. In compression, G20-10 exhibited a smoother and progressively increasing response, which is consistent with a gradual collapse sequence. Under impact, this translated into a localized indentation mode with crater depths of 3.48–4.11 mm and preservation of the overall core integrity. In contrast, G14-14 exhibited face bending and partial delamination of the Kevlar/PLA top sheet. Thus, although G14-14 performed very well in global compression, G20-10 was more effective in

localized impact, as the denser region placed on the impact side improved local strength and limited the spread of damage.

The re-entrant architectures also exhibited consistent behaviour in the two tests. In quasi-static compression, RE and RE var exhibited lower stiffness and lower SEA than the gyroid configurations, which is consistent with bending-dominated cell wall deformation. This response was reproduced in impact, where both re-entrant architectures suffered complete structural collapse. RE specimens developed low peak impact forces but very large displacements, indicating that the structure dissipated energy primarily through extensive deformation and collapse. This confirms that the uniform re-entrant architecture is effective in attenuating the transmitted force, but does so at the expense of structural integrity.

The graded re-entrant architecture, RE var, exhibited a more controlled response than the uniform RE configuration. Under compression, RE var exhibited a lower initial peak stress but a larger mid-stroke plateau compared to RE, suggesting that the grading promoted a more progressive collapse front. Under impact, RE var also exhibited a more repeatable response and a much smaller maximum displacement than RE. This indicates that the grading strategy improved the stability of the re-entrant response and restricted the deformation stroke. However, as the specimens still failed by complete collapse, the quasi-static improvement did not translate into sufficient post-impact integrity at 100 J. Therefore, for the re-entrant topology, grading improved collapse control but did not prevent catastrophic failure under localized dynamic loading.

4. Conclusions

This work investigated the influence of network topology and functional grading on the quasi-static compression and low-velocity impact behaviour of PLA lattice core sandwich specimens reinforced with aramid/epoxy face sheets. Four architectures were compared: a uniform gyroid structure (G14-14), a linear graded gyroid structure (G20-10), a uniform re-entrant structure (RE), and a graded re-entrant structure (RE var). All cores were fabricated with similar dimensions and an approximately constant relative density of 0.31, allowing the observed differences in mechanical response to be attributed primarily to topology and grading, rather than mass effects.

Quasi-static compression tests showed that gyroid-based architectures provided the most stable and energy-efficient response. Both G14-14 and G20-10 exhibited higher stiffness, higher plateau stress, and higher specific energy absorption than the re-entrant architectures. The gyroid cores achieved SEA values of 3.66–4.09 J/g up to 50% nominal strain, approximately double the values obtained for the re-entrant cores. This confirms that the continuous network of TPMS walls promotes a more efficient load transfer mechanism and more stable progressive collapse under compression.

Functional grading modified the collapse response within both families. In the gyroid structures, grading reduced the initial peak stress while maintaining a comparable plateau stress, indicating a smoother transition from the initial loading stage to progressive collapse. In re-entrant structures, grading had an even stronger effect, significantly reducing the initial peak stress and promoting a more progressive increase in stress. Therefore, grading by cell size can be used as an effective design parameter to control the onset and spatial progression of collapse.

Low-velocity impact tests confirmed the topology-dependent hierarchy observed under quasi-static compression, but also highlighted the importance of local indentation, the interaction between the impacted face sheet and the lattice core, and post-impact integrity. The gyroid specimens retained their overall structural integrity after the 100 J impact, whereas the re-entrant specimens suffered complete collapse. The G20-10 graded gyroid exhibited the most favorable impact behaviour, combining the highest and most repeatable peak impact force with localized indentation and limited damage spread. The uniform gyroid G14-14 also resisted complete collapse, but the impact damage was associated with bending and partial detachment of the upper Kevlar/PLA face sheet.

The re-entrant configurations reduced the transmitted impact force, but this came at the cost of severe structural damage. The uniform RE samples exhibited large deformation and complete collapse, while the RE var configuration improved repeatability and reduced peak displacement. However, the RE var still failed to maintain core integrity under the imposed impact energy. This indicates that re-entrant architectures may be suitable for energy absorption and force attenuation, but are less suitable when residual structural integrity after impact is required.

5. Contact Author Email Address

mailto: cristea.george@incas.ro

6. Copyright Statement

The authors confirm that they, and/or their company or organization, hold copyright on all of the original material included in this paper. The authors also confirm that they have obtained permission, from the copyright holder of any third party material included in this paper, to publish it as part of their paper. The authors confirm that they give permission, or have obtained permission from the copyright holder of this paper, for the publication and distribution of this paper as part of the ICAS proceedings or as individual off-prints from the proceedings.

References

[1] A. Nazir, K. M. Abate, A. Kumar, and J. Y. Jeng, "A state-of-the-art review on types, design, optimization, and additive manufacturing of cellular structures," *International Journal of Advanced Manufacturing Technology*, vol. 104, no. 9–12, pp. 3489–3510, Oct. 2019, doi: 10.1007/s00170-019-04085-3.

[2] Y. Li, D. Jiang, R. Zhao, X. Wang, L. Wang, and L.-C. Zhang, "High Mechanical Performance of Lattice Structures Fabricated by Additive Manufacturing," *Metals (Basel).*, vol. 14, no. 10, p. 1165, Oct. 2024, doi: 10.3390/met14101165.

[3] N. A. Fleck, V. S. Deshpande, and M. F. Ashby, "Micro-architectured materials: past, present and future," *Proceedings of the Royal Society A: Mathematical, Physical and Engineering Sciences*, vol. 466, no. 2121, pp. 2495–2516, Sep. 2010, doi: 10.1098/rspa.2010.0215.

[4] H. Yin, W. Zhang, L. Zhu, F. Meng, J. Liu, and G. Wen, "Review on lattice structures for energy absorption properties," *Compos. Struct.*, vol. 304, p. 116397, Jan. 2023, doi: 10.1016/j.compstruct.2022.116397.

[5] T. D. Ngo, A. Kashani, G. Imbalzano, K. T. Q. Nguyen, and D. Hui, "Additive manufacturing (3D printing): A review of materials, methods, applications and challenges," *Compos. B Eng.*, vol. 143, pp. 172–196, Jun. 2018, doi: 10.1016/j.compositesb.2018.02.012.

[6] I. Gibson, D. Rosen, B. Stucker, and M. Khorasani, *Additive Manufacturing Technologies*. Cham: Springer International Publishing, 2021. doi: 10.1007/978-3-030-56127-7.

[7] J. Zhang, G. Lu, and Z. You, "Large deformation and energy absorption of additively manufactured auxetic materials and structures: A review," *Compos. B Eng.*, vol. 201, p. 108340, Nov. 2020, doi: 10.1016/j.compositesb.2020.108340.

[8] I. Maskery *et al.*, "Insights into the mechanical properties of several triply periodic minimal surface lattice structures made by polymer additive manufacturing," *Polymer (Guildf).*, vol. 152, pp. 62–71, Sep. 2018, doi: 10.1016/j.polymer.2017.11.049.

[9] F. S. L. Bobbert *et al.*, "Additively manufactured metallic porous biomaterials based on minimal surfaces: A unique combination of topological, mechanical, and mass transport properties," *Acta Biomater.*, vol. 53, pp. 572–584, Apr. 2017, doi: 10.1016/j.actbio.2017.02.024.

[10] O. Al-Ketan and R. K. Abu Al-Rub, "Multifunctional Mechanical Metamaterials Based on Triply Periodic Minimal Surface Lattices," *Adv. Eng. Mater.*, vol. 21, no. 10, Oct. 2019, doi: 10.1002/adem.201900524.

[11] M. Leary *et al.*, "Selective laser melting (SLM) of AlSi12Mg lattice structures," *Mater. Des.*, vol. 98, pp. 344–357, May 2016, doi: 10.1016/j.matdes.2016.02.127.

[12] I. Maskery *et al.*, "A mechanical property evaluation of graded density Al-Si10-Mg lattice structures manufactured by selective laser melting," *Materials Science and Engineering: A*, vol. 670, pp. 264–274, Jul. 2016, doi: 10.1016/j.msea.2016.06.013.

[13] S. Y. Choy, C.-N. Sun, K. F. Leong, and J. Wei, "Compressive properties of functionally graded lattice structures manufactured by selective laser melting," *Mater. Des.*, vol. 131, pp. 112–120, Oct. 2017, doi: 10.1016/j.matdes.2017.06.006.

[14] O. Al-Ketan, D.-W. Lee, R. Rowshan, and R. K. Abu Al-Rub, "Functionally graded and multi-morphology sheet TPMS lattices: Design, manufacturing, and mechanical properties," *J. Mech. Behav. Biomed. Mater.*, vol. 102, p. 103520, Feb. 2020, doi: 10.1016/j.jmbbm.2019.103520.

[15] W. E. Frazier, "Metal Additive Manufacturing: A Review," *J. Mater. Eng. Perform.*, vol. 23, no. 6, pp. 1917–1928, Jun. 2014, doi: 10.1007/s11665-014-0958-z.

[16] D. W. Abueidda, M. Elhebeary, C.-S. (Andrew) Shiang, S. Pang, R. K. Abu Al-Rub, and I. M. Jasiuk, "Mechanical properties of 3D printed polymeric Gyroid cellular structures: Experimental and finite element study," *Mater. Des.*, vol. 165, p. 107597, Mar. 2019, doi: 10.1016/j.matdes.2019.107597.

[17] L. Yang, R. Mertens, M. Ferrucci, C. Yan, Y. Shi, and S. Yang, "Continuous graded Gyroid cellular structures fabricated by selective laser melting: Design, manufacturing and mechanical properties," *Mater. Des.*, vol. 162, pp. 394–404, Jan. 2019, doi: 10.1016/j.matdes.2018.12.007.

[18] D. Li, W. Liao, N. Dai, and Y. M. Xie, "Comparison of Mechanical Properties and Energy Absorption of Sheet-Based and Strut-Based Gyroid Cellular Structures with Graded Densities," *Materials*, vol. 12, no. 13, p. 2183, Jul. 2019, doi: 10.3390/ma12132183.